Ultrasound Speckle Reduction after Coded Excitation and Pulse Compression

Joshua S. Ullom, *Student Member, IEEE*

***Abstract*— A technique for improvement of ultrasonic B-mode imaging that uses coded excitation, pulse compression, and frequency compounding was recently developed. A coded excitation and pulse compression technique known as resolution enhancement compression is used to enhance the bandwidth of an imaging system by a factor of two. This bandwidth can be subdivided into smaller subbands through the speckle-reducing technique known as frequency compounding. Frequency compounded images that are generated using various subband widths were averaged to reduce speckle and to improve contrast while preserving resolution. Further improvements in contrast and reduction in speckle were obtained by applying post-processing despeckling filters. The following post-processing despeckling filters were explored and analyzed in regard to contrast improvement, speckle reduction, and image feature preservation: median, Lee, homogeneous mask area, geometric, and speckle reducing anisotropic diffusion (SRAD). To evaluate the performance of each filter, metrics such as contrast-to-noise ratio, signal-to-noise ratio, mean squared error, and others were calculated for each result. Thirty tissue-mimicking phantoms and some experimental ultrasound images were obtained and filtered. Results indicate that SRAD provided the most improvement and may even improve the image.**

***Index Terms*— Coded excitation, contrast improvement, frequency compounding, pulse compression, speckle reduction, ultrasound**

I. Introduction

ULTRASONIC images are corrupted with system-dependent imperfections called speckle. Seen as the granular or salt and pepper distortions, speckle is multiplicative noise that can mask small or low-contrast lesions. Speckle can be a problem in diagnostic ultrasound, especially in the area of early detection of cancerous lesions. These lesions are often either low-contrast or so small that the effects of speckle make the lesion imperceptible. It is desired to detect tumors as early as possible, and the effects of speckle may inhibit early detection.

The overall quality of ultrasound (US) images can be improved through averaging methods or post-processing. Examples of an averaging method include the use of frequency compounding [1], [2] or spatial compounding [3], [4]. A novel averaging scheme that makes use of coded excitation, pulse compression, and frequency compounding known as eREC-FC (discussed in section II) was used as the starting point for the implementation of post-processing nonlinear filtering because of its ability to improve contrast, reduce speckle, and preserve resolution in the image. Post-processing methods include filtering the resulting image or radio frequency (RF) data. Many filters have been developed to effectively eliminate or reduce speckle in US images, including Lee [5], Kuan [6], and speckle reducing anisotropic diffusion [7].

This study focuses on improving US image quality of eREC-FC (a technique discussed in section II) US images, through post-processing filtering techniques.

Manuscript received April 10, 2010. This work was supported in part by Bradley University, Peoria, IL.

The author is an undergraduate student at Bradley University enrolled in the Department of Electrical and Computer Engineering, Peoria, Illinois 61606 USA (email: jullom@mail.bradley.edu).

II. Background

A. Conventional Ultrasonic Imaging

US imaging begins with the excitation of a transducer with an impulse, which can be focused to a certain distance or unfocused. As the transducer is excited, it emits an ultrasonic pressure wave. This pressure wave is then propagated through a medium, such as tissue. While propagating through the medium, the wave will scatter from objects such as cells, fibers, etc. However, only the backscattered signal, known as the RF echoes, is used to construct the B-mode image.

The constructive and destructive interference of the pressure waves forms speckle in the image. Thus, speckle is an inherent property of the US imaging system, not the subject being imaged.

In conventional US (CP) imaging, a delta function is used to excite the transducer.

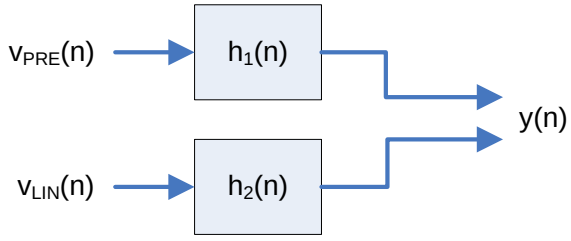

Fig. 1. Convolution equivalence results flow chart.

B. Resolution Enhancement Compression (REC)

REC is a novel coded excitation method of US imaging that uses a pre-enhanced chirp [8]. To obtain a pre-enhanced chirp, convolution equivalence (CE) is used. CE adapts the transducer's impulse response, $h_1(n)$, to a more desirable impulse response, $h_2(n)$, by an appropriately constructed excitation signal. A linear chirp $v_{LIN}(n)$ is used to excite $h_2(n)$, which has been designed to have twice the bandwidth of $h_1(n)$. By using CE shown in (1), a pre-enhanced chirp, $v_{PRE}(n)$, is generated and the equivalence is shown in Fig. 1.

$$v_{LIN}(n) * h_2(n) = v_{PRE}(n) * h_1(n) \quad (1)$$

The distinctive advantage of REC is the improvement in the resolution, as a direct result of $h_2(n)$ having twice the bandwidth of $h_1(n)$, and thus, the resulting transducer response has twice the bandwidth of a CP response. Fig. 2 shows the convolution equivalence for two Gaussian impulse responses based on a real transducer.

C. REC – Frequency Compounding (REC-FC)

Frequency compounding (FC) was implemented on REC [9]. In FC, the spectrum of the RF echo data is subdivided using subband filters to generate partially uncorrelated RF echoes. Then, the generated RF echoes are compounded to reduce the speckle. In the REC-FC study, various subband widths were evaluated. As the subband width became smaller, the variance in the image was reduced but at the expenses of deteriorating the axial resolution. Therefore, the tradeoff in REC-FC was contrast resolution vs. axial resolution.

D. Enhanced REC-FC (eREC-FC)

Another technique known as enhanced REC-FC (eREC-FC), compounds several REC-FC images that were obtained at different subband widths [10]. There are three defining characteristics of eREC-FC. First, the axial resolution in the resulting image is comparable to CP. Second, the contrast resolution is improved over CP by a factor of about two. Finally, speckle in the image is reduced.

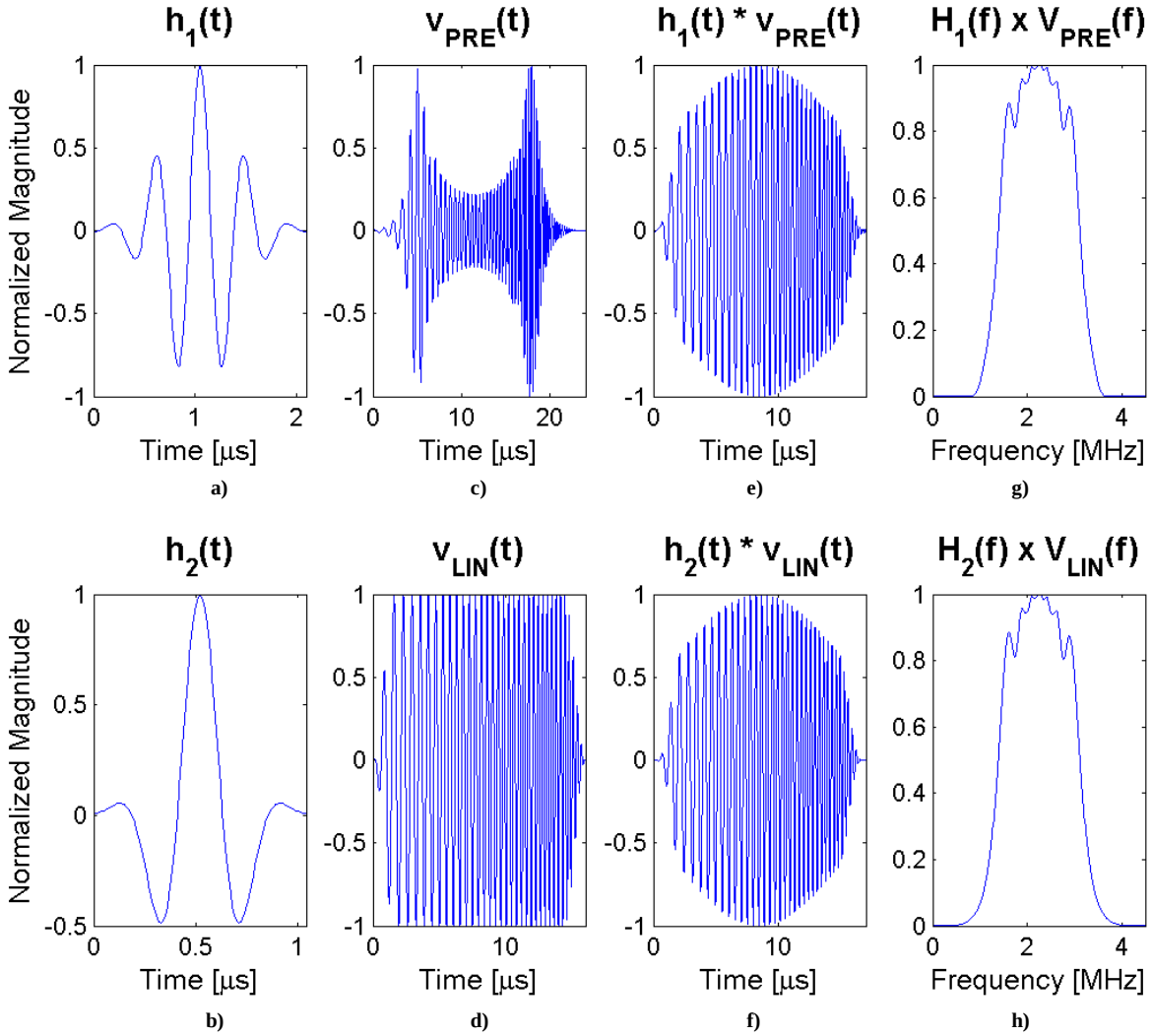

Fig. 2. Simulated impulse responses, chirp functions, convolutions, and spectrums of convolution. (a) Gaussian pulse designed with 48% -3 dB bandwidth. (b) Gaussian pulse designed with 97% -3 dB bandwidth. (c) Pre-enhanced chirp used to excite the 48% bandwidth source. (d) Tapered linear chirp used to excite the 97% bandwidth source. (e) Convolution of pre-enhanced chirp with the 48% bandwidth source. (f) Convolution of tapered linear chirp with the 97% bandwidth source. (g) Spectrum of part e). (h) Spectrum of part f).

III. Methods and Procedures

Images obtained with the eREC-FC technique were further processed with the despeckling filters listed in this section. Most of the following filters make use of a moving, overlapping window. This is defined as a window of size $(n \times n)$, where n is an odd integer that advances through the entire image one pixel at a time. The center pixel of the window is the location that will be adjusted in the filtered image. In the iterative techniques, after the first iteration (filtering of the original image), the filtered image becomes the input to the filter for each successive iteration.

A. Filter Descriptions

Median Filtering: Median filtering makes use of a moving, overlapping window. The median of the pixels in the window is the value of the pixel in the filtered image. Median filtering is used to smooth an image and minimize or eliminate noise spikes, with the idea that all pixels in a small region of an image should be similar. Since the computing the median is a simple calculation, it can also be implemented in a very efficient manner [11].

Local Statistics Filtering: Local statistics filtering also uses a moving, overlapping window. The filter uses statistics within that window such as mean and variance to adjust the center pixel of the window. Specifically, the Lee filter was investigated [5]. The equation that governs this filtering process is [12]

$$f_{i,j} = \bar{g}_{i,j} + k_{i,j} \cdot \left[g_{i,j} - \bar{g}_{i,j}\right] \tag{2}$$

where $f_{i,j}$ is the filtered pixel at location (i,j), $\bar{g}_{i,j}$ is the mean of the pixel intensities in the window, $g_{i,j}$ is the center pixel in the window, and

$$k_{i,j} = \frac{1 - \overline{g_{i,j}}\sigma^2}{\sigma^2(1+\sigma_n^2)} \tag{3}$$

where σ^2 is the variance in the window and σ_n^2 is the noise variance in the whole image. This will result in $k \in [0\ 1]$. Since the variance in noise, or speckle, is not known, it is estimated by

$$\sigma_n^2 = \sum_I \frac{\sigma_{w_b}^2}{\overline{w_b}} \tag{4}$$

where w_b is a window (that is 10 times bigger in this implementation) than the filtering window, $\sigma_{w_b}^2$ and $\overline{w_b}$ are the variance and mean of pixel intensity of the larger window, w_b, respectively. This window moves through the entire image I.

Homogeneous Mask Area Filtering: Two windows are used in homogeneous mask area filtering, a large main window, which determines the pixel location to filter, and a smaller subwindow within the main window [12]. For each subwindow, a speckle index is calculated as

NW	N	NE
W	*	E
SW	S	SE

Fig. 3. Geometric filtering directions.

$$s = \frac{\mu}{\sigma^2} \tag{5}$$

where μ and σ^2 are the mean and variance of the pixel intensity in the window, respectively. The mean of region with the smallest speckle index becomes the filtered pixel value. For this study, the subwindow was $(n-2 \times n-2)$.

Geometric Filtering: Using a moving, overlapping window of size (3×3), the geometric filter uses an iterative approach to make the center pixel of the window more like its neighboring pixels [13]. The idea behind the geometric filter is that a very small region of an image should be homogeneous. There are four directions the geometric filter iterates through – North-South, East-West, Northwest-Southeast, and Northeast-Southwest, as defined in Fig. 3. In each case, a line of three pixels is created.

The algorithm for computing the filtered pixel update is shown, where a is the pixel in the North or West direction, b is always the center pixel, and c is the pixel in the East or South direction [14]

$$\begin{aligned}
&\text{if } a \geq b+2, && b = b+1\\
&\text{if } a > b \leq c, && b = b+1\\
&\text{if } c > b \leq a, && b = b+1\\
&\text{if } c \geq b+2, && b = b+1\\
&\\
&\text{if } a \leq b-2, && b = b-1\\
&\text{if } a < b \geq c\ , && b = b-1\\
&\text{if } c < b \geq a, && b = b-1\\
&\text{if } c \leq b-2, && b = b-1.
\end{aligned} \tag{6}$$

Speckle Reducing Anisotropic Diffusion (SRAD): SRAD is an algorithm that smears the pixel intensities within homogenous regions while preserving edges by not smearing across inhomogeneous regions. SRAD is based on anisotropic diffusion and is used by solving the diffusion equation described as a nonlinear partial differential equation [7]

$$\begin{cases} \dfrac{\partial I}{\partial t} = div[c(|\nabla I|) \cdot \nabla I] \\ I(t=0) = I_0 \end{cases} \tag{7}$$

where div is the divergence operator, ∇ is the gradient operator, I_0 is the original image and is positive and never zero anywhere, and

$$c(x) = \frac{1}{1 + \left(\frac{x}{k}\right)^2} \tag{8}$$

where k is an edge magnitude parameter.

For SRAD, a few adjustments are made to the anisotropic diffusion differential equation [7]. First, the diffusion coefficient is

$$c(q) = \frac{1}{1 + \left(\frac{q^2(i,j;t) - q_0^2(t)}{q_0^2(t) \cdot (1 + q_0^2(t))}\right)} \tag{9}$$

where q is the instantaneous coefficient of variation and q_0, the speckle scale function. q is described by

$$q(i,j;t) = \sqrt{\frac{\frac{1}{2}\left(\frac{\nabla I}{I}\right)^2 - \frac{1}{16}\left(\frac{\nabla^2 I}{I}\right)^2}{\left(1 + \frac{1}{4}\left[\frac{\nabla^2 I}{I}\right]\right)^2}} \tag{10}$$

and q_0 is based on statistics in a region of the image

$$q_0(t) = \frac{\sqrt{\sigma^2_{z(t)}}}{\overline{z(t)^2}} \tag{11}$$

where $\sigma^2_{z(t)}$ and $\overline{z(t)}$ are the variance and mean of pixel intensity over a homogeneous region at time t, respectively. The basis for the SRAD update function is the discrete isotropic diffusion update function, which is described by

$$I_{i,j}^{t+\Delta t} = I_{i,j}^t + \frac{\Delta t}{4}\left(I_{i+1,j}^t + I_{i-1,j}^t + I_{i,j+1}^t + I_{i,j-1}^t - 4I_{i,j}^t\right) \tag{12}$$

which can be viewed as

$$I_{i,j}^{t+\Delta t} = I_{i,j}^t + \frac{\Delta t}{4} d_{i,j}^t \tag{13}$$

where $d_{i,j}^t$ is the divergence function. In SRAD, the calculation of the divergence function in discrete implementation, with discretized spatial and temporal components

$$\begin{aligned} t &= n\Delta t, \quad n = 0,1,2 \ldots \\ x &= ih, \quad i = 0,1,2, \ldots, M-1 \\ y &= jh, \quad j = 0,1,2, \ldots, N-1. \end{aligned}$$

The gradient approximations and Laplacian approximation are computed as

$$\nabla_L I_{i,j}^n = \left[\frac{I_{i+1,j}^n - I_{i,j}^n}{h}, \frac{I_{i,j+1}^n - I_{i,j}^n}{h}\right] \tag{14}$$

$$\nabla_R I_{i,j}^n = \left[\frac{I_{i,j}^n - I_{i-1,j}^n}{h}, \frac{I_{i,j}^n - I_{i,j-1}^n}{h}\right] \tag{15}$$

$$\nabla^2 I_{i,j}^n = \frac{I_{i+1,j}^n + I_{i-1,j}^n + I_{i,j+1}^n + I_{i,j-1}^n - 4I_{i-j}^n}{h} \tag{16}$$

having boundary conditions

$$\begin{aligned} I_{-1,j}^n &= I_{0,j}^n, \ I_{M,j}^n = I_{M-1,j}^n \\ j &= 0,1,2, \ldots, N-1 \end{aligned} \tag{17}$$

$$\begin{aligned} I_{i,-1}^n &= I_{i,0}^n, \ I_{i,N}^n = I_{i,N-1}^n, \\ i &= 0,1,2, \ldots, M-1. \end{aligned} \tag{18}$$

The diffusion coefficient is a function of the instantaneous coefficient of variation, which is a function of the approximated image derivatives and Laplacian

$$c_{i,j}^n = c\left[q\left(\frac{1}{I_{i,j}^n}\sqrt{\left|\nabla_R I_{i,j}^n\right|^2 + \left|\nabla_L I_{i,j}^n\right|^2}, \frac{1}{I_{i,j}^n}\nabla^2 I_{i,j}^n\right)\right]. \tag{19}$$

The divergence of $c(\cdot)\nabla I$ is computed as

$$\begin{aligned} d_{i,j}^n = \frac{1}{h^2}\big[&c_{i+1,j}^n\left(I_{i+1,j}^n - I_{i,j}^n\right) + c_{i,j}^n\left(I_{i-1,j}^n - I_{i,j}^n\right) + \\ &c_{i,j+1}^n\left(I_{i,j+1}^n - I_{i,j}^n\right) + c_{i,j}^n\left(I_{i,j-1}^n - I_{i,j}^n\right)\big] \end{aligned} \tag{20}$$

having boundary conditions

$$\begin{aligned} d_{-1,j}^n &= d_{0,j}^n, \ d_{M,j}^n = d_{M-1,j}^n \\ j &= 0,1,2, \ldots, N-1 \end{aligned} \tag{21}$$

$$\begin{aligned} d_{i,-1}^n &= d, \ d_{i,N}^n = d_{i,N-1}^n, \\ i &= 0,1,2, \ldots, M-1. \end{aligned} \tag{22}$$

Finally, the approximation of the solved differential equation, the SRAD update function, is

$$I_{i,j}^{n+1} = I_{i,j}^n + \frac{\Delta t}{4} d_{i,j}^n \tag{23}$$

In the SRAD implementation, n is an artificial time value that increases by one for every iteration through the SRAD algorithm. The parameters h and Δt were 1 and 0.05, respectively as specified in [7].

The selection of a region z could be automated to minimize subjectivity by using an appropriately-sized moving, overlapping window. The variance was calculated in every window, and the windowed region with the least variance would become z, being the region with the least noise. Also, for US images in which the distance represented by each pixel is different on each axis, the SRAD algorithm was scaled (sSRAD).

This scaling alteration required knowing the actual size of the image in terms of distances. The change between pixels is then calculated for each direction

$$\Delta_j = \frac{i}{p_i} \tag{24}$$

where i is the actual length of the image in the i-direction and p_i is the number of pixels along the i-axis, and Δ_i is computed similarly. Then the scale factors are normalized based on the scale factor with the larger magnitude. The scaling is applied to the divergence equation

$$d_{i,j}^n = \frac{1}{h^2}\left[c_{i+1,j}^n\left(I_{i+1,j}^n - I_{i,j}^n\right)\Delta_i + c_{i,j}^n\left(I_{i-1,j}^n - I_{i,j}^n\right)\Delta_i + c_{i,j+1}^n\left(I_{i,j+1}^n - I_{i,j}^n\right)\Delta_j + c_{i,j}^n\left(I_{i,j-1}^n - I_{i,j}^n\right)\Delta_j\right]. \tag{25}$$

B. Image Quality Metrics

1. Contrast

Contrast-to-Noise Ratio (CNR) quantifies the degree to which one region of an image is visible in comparison to another region. For this study, a region in the lesion is compared to a region in the background. CNR is described as [14]

$$CNR = \frac{|\mu_B - \mu_T|}{\sqrt{\sigma_B^2 + \sigma_T^2}}. \tag{26}$$

Because of attenuation, the CNR was calculated at the same depth for both regions. A larger CNR represents better contrast.

2. Speckle

The comparative signal-to-noise ratio (cSNR) is defined as [15]

$$cSNR = 10\log_{10}\frac{\sum_{i=1}^{M}\sum_{j=1}^{N}\left(g_{i,j}^2 + f_{i,j}^2\right)}{\sum_{i=1}^{M}\sum_{j=1}^{N}\left(g_{i,j} - f_{i,j}\right)^2} \tag{27}$$

and peak SNR (PSNR) is given by [17]

$$PSNR = -10\log_{10}\frac{\sum_{i=1}^{M}\sum_{j=1}^{N}\left(g_{i,j} - f_{i,j}\right)^2}{g_{max}^2} \tag{28}$$

where g is the unfiltered image, f is the filtered image, and g_{max}^2 is the maximum intensity of the unfiltered image.

cSNR and PSNR are a comparative measure between the filtered and the unfiltered images. cSNR quantifies the amount of noise, or speckle, reduction from the unfiltered to the filtered image, with higher results representing a larger improvement. PSNR measures image fidelity, or the similarity of the filtered and unfiltered image. PSNR is larger for better-transformed images, that is, images that better represent the original despite the alterations.

3. Overall Image

A few metrics were used to compute absolute changes in the filtered images. These provide easily-understandable measurements of the differences in the images resulting from filtering. Mean squared error (MSE) computes the mean squared difference of all pixels in the transformation

$$MSE = \frac{1}{MN}\sum_{i=1}^{M}\sum_{j=1}^{N}\left(g_{i,j} - f_{i,j}\right)^2 \tag{29}$$

and root MSE (RMSE) calculates the precision of the transformation

$$RMSE = \sqrt{\frac{1}{MN}\sum_{i=1}^{M}\sum_{j=1}^{N}\left(g_{i,j} - f_{i,j}\right)^2}. \tag{30}$$

When $MSE = RMSE = 0$ there is no average difference between the filtered and unfiltered images. A filter resulting in zero MSE and RMSE could mean all regions of the image (target, background, etc.) were transformed to the mean of that region, or the images are the same.

Additionally, the error summation in the form of the Minkowski metric [16]

$$Err = \left(\frac{1}{MN}\sum_{i=1}^{M}\sum_{j=1}^{N}\left|g_{i,j} - f_{i,j}\right|^{\beta}\right)^{1/\beta} \tag{31}$$

is evaluated at $\beta = 3$ (Err3) and $\beta = 4$ (Err4). When $\beta = 2$, the RMSE is computed. The Minkowski metric measures the norm of the dissimilarity between the original and despeckled images and is a further abstracted measure of the precision of the transformations. Again, $Err = 0$ means there was either no change from the filter or the filtered image was a result of the ideal filtering process.

The universal quality index [17] represents image distortion as a combination of loss of correlation, luminance distortion, and contrast distortion. Universal quality index is defined as

$$Q = \frac{\sigma_{gf}}{\sigma_f\sigma_g}\cdot\frac{2\bar{f}\bar{g}}{\left(\bar{f}\right)^2 + (\bar{g})^2}\cdot\frac{2\sigma_f\sigma_g}{\sigma_f^2 + \sigma_g^2} \tag{32}$$

which can be rewritten as

$$Q = \frac{4\bar{f}\bar{g}\sigma_{gf}}{\left(\bar{f}^2 + \bar{g}^2\right)\left(\sigma_f^2 + \sigma_g^2\right)} \tag{33}$$

where $\bar{f}$ and $\bar{g}$ are the mean of the filtered and unfiltered values, with standard deviations, σ_f and σ_g, and variances, σ_f^2 and σ_g^2, respectively, and σ_{gf} is the covariance between the original and despeckled windows. To compute Q, a sliding, non-overlapping (8×8) window was used. The average of each windowed region for the entire image was computed. Q is bounded such that $-1 \le Q \le 1$, where $Q = 1$ if $g_{i,j} = f_{i,j}$ and $Q = -1$ if $f_{i,j} = 2\bar{g} - g_{i,j}$.

Finally, the structural similarity index between two images [17], which is a generalized form of the universal quality index, is computed as

$$SSIM = \frac{(2\bar{f}\bar{g} + c_1)(2\sigma_{gf} + c_2)}{(\bar{f}^2 + \bar{g}^2 + c_1)(\sigma_f^2 + \sigma_g^2 + c_2)} \quad (34)$$

where $c_1 = 0.01dr$ and $c_2 = 0.03dr$, with dr representing the dynamic range of the ultrasound images. SSIM is bounded such that $-1 \leq SSIM \leq 1$, where $SSIM = 1$ for a good similarity and $SSIM = -1$ for a poor similarity between the filtered and unfiltered images.

C. Computer Simulations

Computer simulations were performed in MATLAB (MathWorks, Natick, MA) to generate all US images [11]. The simulations used the following received pulse-echo pressure field model [14]

$$g'(x, y, t) = h_1(t) * f(x, y) * h_{pe}(y, t) \quad (35)$$

where x is the axial spatial coordinate, y is the lateral spatial coordinate, $h_1(t)$ is the pulse-echo impulse response of the transducer, $f(x, y)$ is the scattering function, and $h_{pe}(y, t)$ is the modified pulse-echo spatial impulse response to take into account the geometry of the transducer in respect to the scattered beam field (beam diffraction). To generate the pulse-echo impulse response $h_1(t)$ in conventional imaging, a sinusoid of four cycles is gated with a Hanning window

$$w(n) = \begin{cases} \frac{1}{2}\left(1 - \cos\left(\frac{2\pi n}{L_H - 1}\right)\right), & 0 \leq n \leq L_H - 1 \\ 0, & \text{otherwise} \end{cases} \quad (36)$$

where n is an integer and is the number of samples in the window. The parameters of the window and sinusoid were chosen to match the transducer used in experiments. The resulting pulse-echo impulse response generated is located at the focus of a 2.25 MHz single-element transducer (f/2.66) with a fractional bandwidth of 50% at –3 dB, with a corresponding window length of $n = 128$. For REC, the desired impulse response function $h_2(t)$ was constructed to have double the fractional bandwidth (100%) at –3 dB, which uses a window of length of $n = 64$. The spatial response of a circular focused piston source can be simulated as a circular Gaussian beam defined as

$$h_{pe}(y, t) = \delta\left(t - \frac{2R_d}{c}\right) e^{-\frac{y^2}{\sigma_y^2}} \quad (37)$$

where R_d is the distance from the source to target in space, c is the speed of sound of the medium, and σ_y is the nominal lateral beamwidth of the source at –6 dB and is equal to 1.28 mm.

The transducer was laterally translated in increments of 0.1 mm, and the received RF backscatter data were sampled at a rate of 100 MHz. The RF backscatter data have a size of 4096×58 samples, axially and laterally. The object being imaged was a cylindrical target with a radius of 7.5 mm, located at the center of the simulated phantom, which was 20 mm long, 30 mm wide, and 1.92 mm high. The amplitude of the scatterers in the target were twice that of those in the background in order to cause the target to have a contrast of approximately +6 dB. The phantom contains an average of 20 point scatterers per resolution cell volume, in order to ensure fully developed speckle, and were uniformly distributed throughout the phantom.

IV. Simulation Results

Thirty phantoms were simulated, imaged, and filtered using MATLAB. All filters described in section III-A were applied to each conventional and eREC-FC images. The window-based filters were all applied with window sizes of n = 3, 5, 7, 9, and 11. The geometric filter was applied in iterations of 1 through

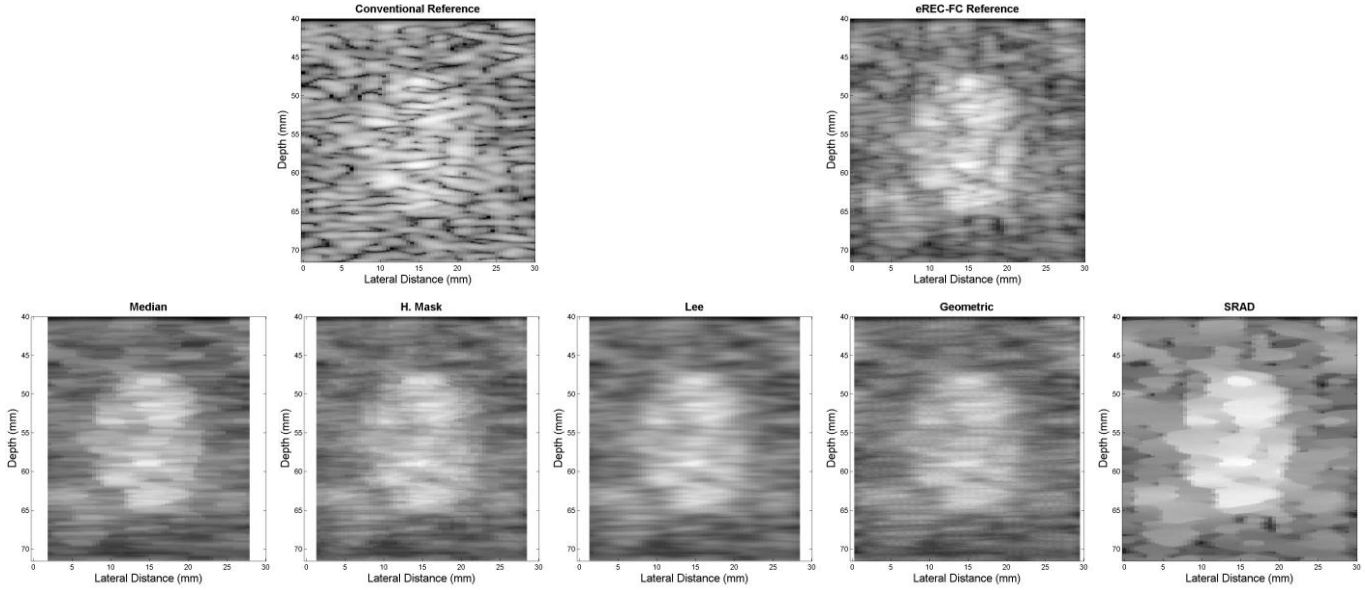

Fig. 4. An example of results of filtering simulation images. Top row – conventional and eREC-FC reference images. Bottom row – median filter (9), homogeneous mask area filter (7), Lee filter (7), geometric filter (5), sSRAD (3300). Parenthesis denote (n x n) window or n iterations.

	eREC-FC	Med			HMA			Lee			Geo			sSRAD		
		3	7	11	5	7	11	3	7	11	1	5	9	900	2100	3300
CNR	2.0	2.9	3.5	3.9	3.2	3.6	4.0	2.9	3.6	4.1	3.0	3.6	3.3	3.8	4.7	5.3
SNR	10.4	10.2	9.9	9.7	10.1	9.9	9.6	10.3	9.9	9.7	10.3	10.9	11.4	17.7	17.3	17.0
PSNR	16.2	16.1	15.8	15.5	15.9	15.7	15.5	16.1	15.8	15.5	16.1	16.5	16.8	18.7	18.2	17.8
MSE	39.2	40.1	43.1	45.4	41.7	43.5	45.9	40.0	42.9	45.5	39.5	36.3	33.6	22.9	25.6	28.0
RMSE	6.2	6.3	6.5	6.7	6.4	6.6	6.8	6.3	6.5	6.7	6.3	6.0	5.8	4.8	5.1	5.3
Err3	7.8	7.9	8.2	8.4	8.1	8.2	8.4	7.9	8.2	8.4	7.9	7.7	7.4	6.0	6.4	6.6
Err4	9.3	9.4	9.7	9.9	9.6	9.7	10	9.4	9.7	9.9	9.4	9.2	8.9	7.3	7.7	7.9
Q	0.47	0.44	0.30	0.17	0.28	0.22	0.12	0.43	0.25	0.12	0.40	0.22	0.11	0.46	0.38	0.34
SSIM	0.53	0.51	0.39	0.28	0.37	0.32	0.24	0.49	0.35	0.24	0.47	0.32	0.23	0.52	0.46	0.43

Fig. 5.Quantitative simulation results of filtering techniques over the span of window sizes or iterations. The average CNR for the conventional image was 0.8.

9. sSRAD was applied in iterations of $300n$, for n defined above. The performance of each filter was assessed by applying the image quality metrics described in section III-B.

All filters showed qualitative smearing across the entire image except sSRAD, which did not smear across feature edges. Fig. 4 shows the effects of each filter qualitatively on a conventional image as well as on an eREC-FC image of the same phantom. The quantitative results of the metrics averaged over the 30 simulations are shown in Fig. 5. All results in this section are in terms of the average of the 30 simulations.

For every filter except geometric, the largest window or number of iterations resulted in the best CNR. The CNR improvement from geometric filtering peaks at 6 iterations. Furthermore, a larger window does not always significantly improve the CNR. The increase in CNR as a function of window size or iterations follows a logarithmic-like shape. Eventually, the benefit of increasing the window size or iterations will become minimal, in addition to the drawback of an increase in computational time. The eREC-FC technique exhibited 150% CNR improvement on CP images. The largest average percent improvement of CNR from each filter on top of the CNR eREC-FC image improvement was 95%, 100%, 105%, 80%, and 165% for median, homogeneous mask area, Lee, geometric, and sSRAD, respectively. The largest total CNR improvement (from CP image to filtered eREC-FC image) for each filter was 388%, 400%, 413%, 350%, and 563% for median, homogeneous mask area, Lee, geometric, and sSRAD, respectively.

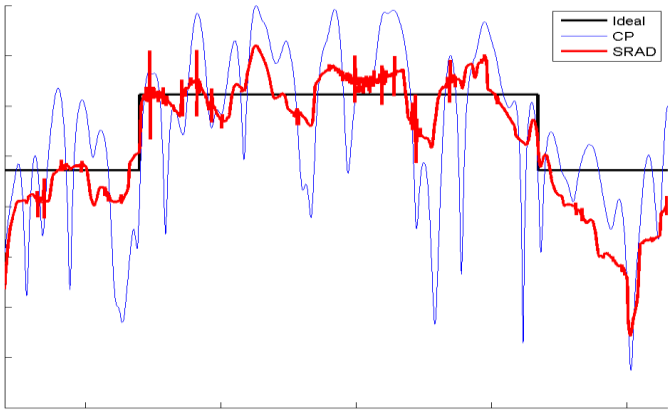

Fig. 6. Comparative axial profile of simulated data. Black, blue, and red denote ideal, conventional pulsing, and sSRAD axial profiles, with depth on the abscissa and magnitude on the ordinate.

sSRAD exhibited an improvement in cSNR and PSNR for all iterations and geometric showed the improvement for all iterations after one. Every filter had a decreasing trend in SNR as the iterations or window size decreased, except geometric, which had an increasing trend. Based on this metric, the order of the filters in respect to improvement was sSRAD, Lee, median, then homogeneous mask area. The geometric filter was left out because its improving trend cannot be compared on the whole to the decreasing trend of the other filters.

Again, sSRAD and geometric filters had better (lower) MSE, RMSE, Err3, and Err4 than the eREC-FC technique; however, the geometric filter was higher than eREC-FC in the case of one iteration. All filters except geometric showed a decreasing trend in performance in all of these metrics. The geometric filter improved as the iterations increased. A comparison of each filter was as follows: sSRAD, geometric, Lee, median, followed by homogeneous mask area.

None of the filters end up improving Q or SSIM. The order of filters in respect to these metrics' performance as a factor of the speed of degradation as window size or iterations increased was: sSRAD, geometric, median, Lee, homogeneous mask area.

The axial profile through the center of the lesion from one of the tissue-mimicking phantoms of the ideal, CP, and sSRAD-filtered images were compared as shown in Fig. 6. The CP profile varies greatly around each region (target, background) and is difficult to properly classify. sSRAD has a reduced variance in the target region. However, a bias was introduced in the background region. This would help explain the increases in CNR achieved with sSRAD.

V. Experimental Results

Three images were obtained experimentally with a transducer with the specifications described in section III-C. Two of these images are of a +6 dB lesion, one having a target of 5 mm and the other with a target of 12 mm, and the third is of a +3 dB contrast, 12 mm lesion. All filters were applied to these experimentally-obtained images in MATLAB. Fig. 7 a) shows the effects of the filters on the 12 mm +6 dB lesion and b) shows the results on the 12mm +3 dB lesion.

Just as in simulation, all filters resulted in smearing across the entire image, except sSRAD, which stopped at feature edges. Because the general trends of the experimental data are

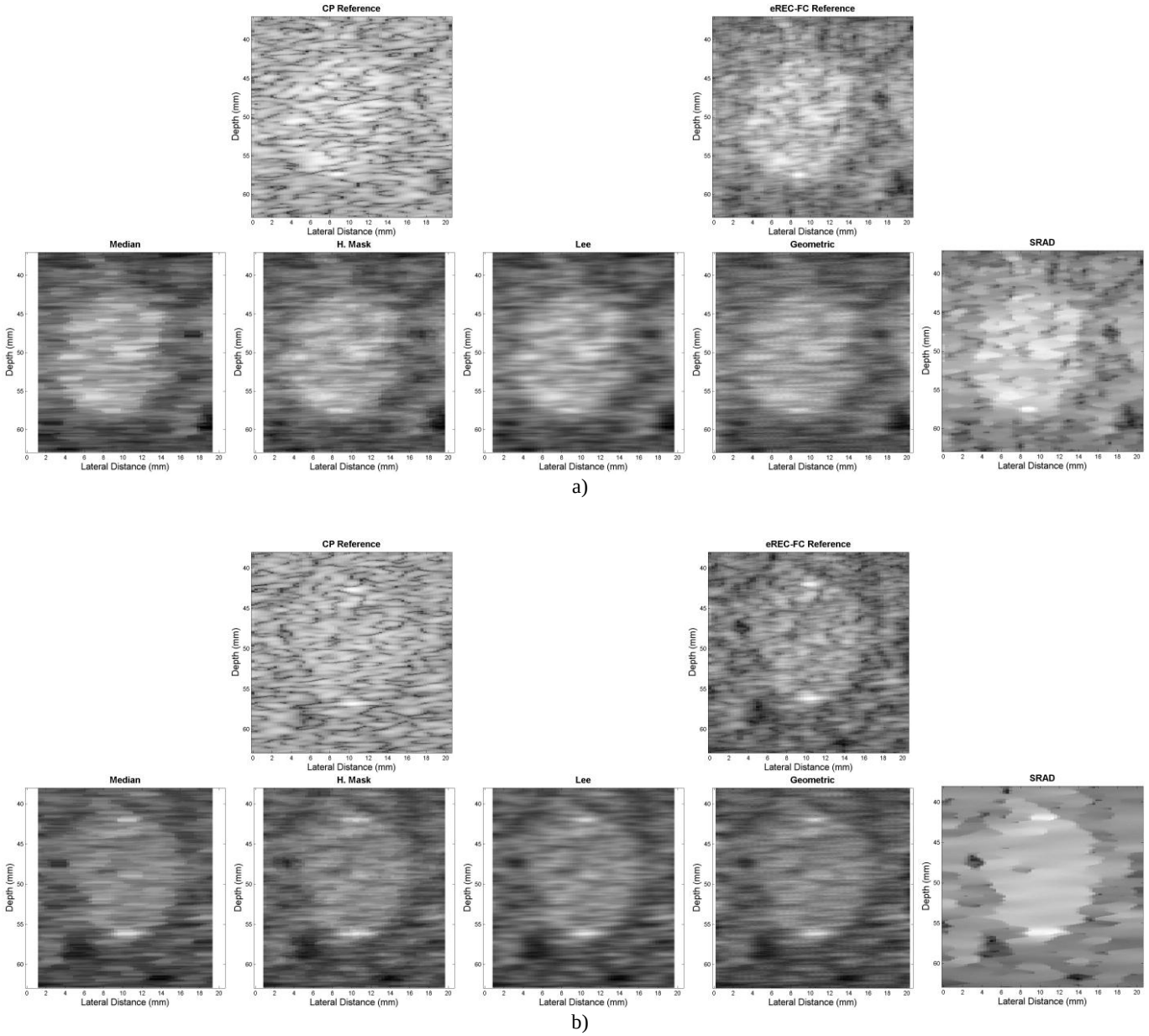

Fig. 7. Qualitative experimental results. a) +6 dB contrast 12 mm data. b) +3 dB contrast 12 mm data. Top rows – conventional and eREC-FC reference images. Bottom rows – median filter (9), homogeneous mask area filter (7), Lee filter (7), geometric filter (5), sSRAD (3300). Parenthesis denote (n x n) window or n iterations.

similar to the simulation, highlights of the experimental results are divided into sections for each image below.

1. 5 mm +6 dB lesion

The best total CNR improvements in this experiment were seen with sSRAD and median filtering, with a CNR improvement of 460% and 453%, respectively, over CP. Geometric and sSRAD had the best results in terms of cSNR with 21% and 78% improvements over eREC-FC, respectively. The two filters with the best MSE results were geometric and sSRAD with 29% and 61% improvements over eREC-FC respectively. Fig. 8 shows quantitative results of all experimental data.

2. 12 mm +6 dB lesion

The best performing filters for CNR in this case were homogeneous mask area and Lee with 350% and 361% respective improvements over CP. Again, geometric and sSRAD had the best cSNR improvements over eREC-FC with 15% and 110%, respectively. The best MSE improvements over eREC-FC were seen in geometric and sSRAD with a 20% and a 59% decrease, respectively.

3. 12 mm +3 dB lesion

Again, CNR improvements were the greatest in homogeneous mask area and Lee, showing 280% and 285% increases over CP, respectively. cSNR results showed that geometric and sSRAD were the best with 20% and 87%

	eREC-FC	Med			HMA			Lee			Geo			sSRAD		
		3	7	11	5	7	11	3	7	11	1	5	9	900	2100	3300
CNR	4.2	4.8	5.9	7.0	4.6	5.0	5.4	4.9	5.6	5.9	4.8	6.0	6.7	5.7	6.6	7.1
SNR	8.7	8.6	8.6	8.6	8.8	8.7	8.6	8.7	8.7	8.7	8.8	9.6	10.5	15.2	15.4	15.0
PSNR	14.8	14.8	14.7	14.7	14.9	14.8	14.8	14.8	14.8	14.8	14.9	15.5	16.3	16.8	17.0	16.7
MSE	82.7	83.3	83.9	84.4	81.2	82.4	83.2	82.3	82.3	82.9	80.8	70.0	58.8	34.8	33.0	35.7
RMSE	9.1	9.1	9.2	9.2	9.0	9.1	9.1	9.1	9.1	9.1	9.0	8.4	7.7	5.9	5.7	6.0
Err3	10.7	10.7	10.7	10.8	10.6	10.7	10.7	10.7	10.7	10.7	10.6	10.0	9.4	6.7	6.6	6.8
Err4	12.2	12.2	12.2	12.3	12.1	12.2	12.2	12.2	12.2	12.2	12.1	11.6	11.0	7.5	7.3	7.4
Q	0.14	0.13	0.09	0.05	0.09	0.07	0.04	0.13	0.08	0.04	0.12	0.08	0.04	0.19	0.20	0.20
SSIM	0.21	0.21	0.17	0.14	0.17	0.16	0.14	0.21	0.17	0.14	0.20	0.17	0.14	0.27	0.28	0.29

a)

	eREC-FC	Med			HMA			Lee			Geo			sSRAD		
		3	7	11	5	7	11	3	7	11	1	5	9	900	2100	3300
CNR	1.6	1.7	2.0	2.3	2.1	2.3	2.5	1.8	2.3	2.6	1.8	2.1	1.8	1.7	1.8	1.9
SNR	8.7	8.6	8.3	8.1	8.5	8.3	8.1	8.6	8.4	8.1	8.7	9.3	10.1	17.3	18.1	18.3
PSNR	16.6	16.5	16.3	16.1	16.4	16.3	16.1	16.6	16.3	16.1	16.6	17.0	17.6	17.8	18.5	18.7
MSE	54.2	55.6	59.1	61.8	56.6	58.8	61.5	55.0	58.5	61.2	54.3	49.3	43.6	27.4	23.3	22.3
RMSE	7.4	7.5	7.7	7.9	7.5	7.7	7.8	7.4	7.6	7.8	7.4	7.0	6.6	5.2	4.8	4.7
Err3	9.0	9.1	9.4	9.6	9.2	9.4	9.6	9.0	9.3	9.6	9.0	8.8	8.4	5.9	5.6	5.5
Err4	10.6	10.7	11.0	11.2	10.8	11.0	11.2	10.7	11.0	11.2	10.7	10.5	10.1	6.5	6.3	6.3
Q	0.40	0.36	0.21	0.10	0.22	0.17	0.08	0.35	0.18	0.08	0.32	0.16	0.06	0.53	0.50	0.48
SSIM	0.45	0.42	0.29	0.20	0.30	0.25	0.18	0.41	0.27	0.18	0.39	0.25	0.17	0.59	0.57	0.55

b)

	eREC-FC	Med			HMA			Lee			Geo			sSRAD		
		3	7	11	5	7	11	3	7	11	1	5	9	900	2100	3300
CNR	1.1	1.1	1.4	1.7	1.4	1.5	1.8	1.2	1.6	1.8	1.2	1.4	1.3	1.4	1.7	1.8
SNR	9.1	9.0	9.0	9.1	9.2	9.2	9.2	9.1	9.2	9.2	9.2	10.0	10.9	14.9	16.4	16.9
PSNR	15.8	15.8	15.8	15.8	16.0	15.9	15.9	15.8	15.9	15.9	15.9	16.5	17.2	16.1	17.3	17.7
MSE	69.3	69.4	69.3	68.4	66.6	67.2	67.1	68.4	67.2	66.7	67.1	58.2	49.7	40.3	30.6	28.2
RMSE	8.3	8.3	8.3	8.3	8.2	8.2	8.2	8.3	8.2	8.2	8.2	7.6	7.0	6.3	5.5	5.3
Err3	10.0	10.0	10.0	10.0	9.9	9.9	9.9	10.0	9.9	9.9	9.9	9.4	8.8	7.3	6.5	6.4
Err4	11.6	11.6	11.6	11.6	11.5	11.5	11.5	11.6	11.5	11.5	11.5	11.0	10.4	8.1	7.5	7.4
Q	0.05	0.05	0.05	0.04	0.05	0.05	0.04	0.05	0.05	0.04	0.05	0.05	0.04	0.07	0.06	0.05
SSIM	0.13	0.13	0.14	0.14	0.13	0.14	0.14	0.13	0.14	0.14	0.13	0.14	0.14	0.17	0.19	0.18

c)

Fig. 8. Quantitative experimental results of filtering techniques over the span of window sizes or iterations. a) +6 dB 5 mm lesion. The average CNR for the conventional image was 1.3. b) +6 dB 12 mm lesion. The average CNR for the conventional image was 0.6. c) +3 dB 12 mm lesion. The average CNR for the conventional image was 0.5.

increases over eREC-FC. Finally, the results of MSE analysis revealed that geometric and sSRAD performed the best with a respective 28% and 59% decrease as compared to eREC-FC. Fig. 8 shows the quantitative data on all experimental results.

The axial profile through the center of the lesion from one of the tissue-mimicking phantoms of the ideal, CP, and sSRAD-filtered images were compared for the experimental +3 dB contrast results to emphasize the need for the reduction of speckle, as shown in Fig. 9. The only difference between Fig. 9 and Fig. 6 is that the contrast of the target is smaller. Consequently, speckle can mask the lesion background line. In Fig. 9, the CP profile varies greatly around each region (target, background) and is significantly difficult to properly classify. sSRAD has a reduced variance in the target region. However, a bias was introduced in the background region, which helps explain the increase in CNR achieved. It is still difficult to

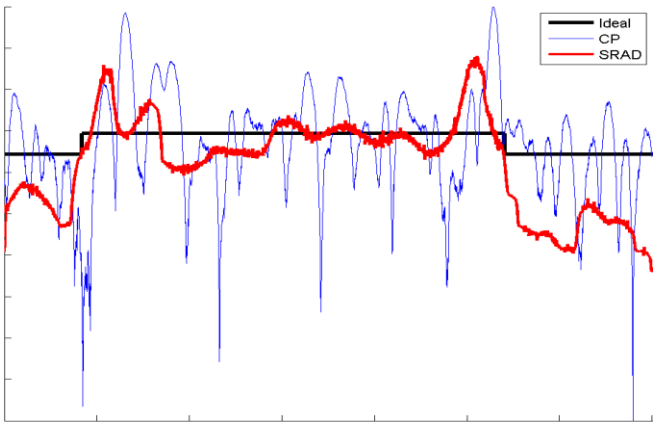

Fig. 9. Comparative axial profile of +3 dB data. Black, blue, and red denote ideal, conventional pulsing, and sSRAD axial profiles, with depth on the abscissa and magnitude on the ordinate.

classify regions appropriately, but there is a small region where a threshold could be set.

VI. Discussion and Conclusion

In simulation and experimental applications, sSRAD resulted in the highest overall improvement. It did not result in the highest improvement in terms of CNR in the 12 mm +6 dB, where it was second-to-last in performance, or 12 mm +3 dB experimental results, where it was only 5% below homogeneous mask area. In all other measures, however, it outperformed the other filters, and often to a significant degree. It is of importance to note that the sSRAD algorithm's improvements come at an increased cost in computational complexity and time.

A possible extension of this work would be segmentation. The resulting image after eREC-FC and SRAD filtering could be used to detect edges more accurately than CP or even eREC-FC. With this benefit, segmenting techniques could be used to superimpose the edges of the object on the CP or eREC-FC image.

Another route would be to implement SRAD in hardware [19], so that it would be a part of the US system. The system could be designed to switch between CP, eREC-FC, and SRAD-filtered, based on what is type of image is desired. This system could also be designed to include the segmentation discussed above.

It is clear that the quality of US images obtained through the eREC-FC technique can be significantly improved through the application of post-processing despeckling filters.

Acknowledgment

The author would like to acknowledge the incredibly helpful discussions and technical assistance of Dr. Jose Sanchez of Bradley University, Peoria, Illinois.

References

[1] S. M. Gehlbach and F. G. Sommer, "Frequency diversity speckle processing," *Ultrason. Imaging*, vol. 9, pp. 92-105, Apr. 1987.

[2] P. A. Magnin, O. T. von Ramm, and F. L. Thurstone, "Frequency compounding for speckle contrast reduction in phased array images," *Ultrason. Imaging*, vol. 4, pp. 267-281, Jul. 1982.

[3] S. K. Jespersen, J. E. Wilhjelm, and H. Sillensen, "Multi-angle compound imaging," *Ultrason. Imaging*, vol. 20, no. 2, pp. 81-102, Apr. 1998.

[4] A. R. Groves and R. N. Rohling, "Two-dimensional spatial compounding with warping," *Ultrasound Med. Biol.*, vol. 30, no. 7, pp. 929-942, Jul. 2004.

[5] J. S. Lee, "Digital image enhancement and noise filtering by using local statistics," *IEEE Trans. Pattern Anal. Machine Intell.*, vol. PAM1-2, 1980.

[6] D. T. Kuan, A. A. Sawchuk, T. C. Strand, and P. Chavel, "Adaptive restoration of images with speckle," *IEEE Trans. Acoust., Speech, Signal Processing*, vol. ASSP-35, pp. 373–383, 1987.

[7] Y. Yu and S. T. Acton, "Speckle reducing anisotropic diffusion," *IEEE Trans. Image Process.*, vol. 11, no. 11, pp. 1260-1270, Nov. 2002.

[8] M. L. Oelze, "Bandwidth and resolution enhancement through pulse compression," *IEEE Trans. Ultrason., Ferroelectr. Freq. Contr.*, vol. 54, no. 4, p. 770, Apr 2007.

[9] J. R. Sanchez and M. L. Oelze, "An ultrasonic imaging speckle-suppression and contrast enhancement technique by means of frequency compounding and coded excitation," *IEEE Trans. Ultrason. Ferroelectr. Freq. Control*, vol. 56, pp. 1327-1339, Jul. 2009.

[10] J. R. Sanchez, "Improving ultrasound imaging using novel coded excitation techniques," Ph.D. dissertation, University of Illinois at Urbana-Champaign, Urbana, IL, USA, 2010.

[11] M. O. Ahmad and D. Sundararajan, "A fast algorithm for two-dimensional median filtering," *IEEE Trans. Circuits and Syst.*, vol. CAS-34, no. 11, pp. 1364-1374, Nov. 1987.

[12] C. P. Loizou, C. Christodoulou, C. S. Pattichis, R. Istepanian, M. Pantziaris, and A. Nicolaides. "Speckle reduction in ultrasound images of atherosclerotic carotid plaque," *14th International Conference on Digital Signal Processing, 2002*, vol. 2, pp. 525-528, 2002.

[13] L. J. Busse, T. R. Crimmins, and J. R. Fienup, "A model based approach to improve the performance of the geometric filtering speckle reduction algorithm," *IEEE Ultrason. Symposium*, pp. 1353-1356, 1995.

[14] M. S. Patterson and F. S. Foster, "The improvement and quantitative assessment for B-Mode images produced by an annular array / cone hybrid," *Ultrason. Imag.*, vol. 5, no. 3, pp. 195-213, Jul. 1983.

[15] D. Sakrison, "On the role of observer and a distortion measure in image transmission," *IEEE Trans. Commun.*, vol.25, pp. 1251-1267, Nov. 1977.

[16] Z. Wang, A. Bovik, H. Sheikh, and E. Simoncelli, "Image quality assessment: From error measurement to structural similarity," *IEEE Trans. Image Processing*, vol. 13, no. 4, pp. 600-612, Apr. 2004.

[17] Z. Wang and A. Bovik, "A universal quality index," *IEEE Signal Processing Lett*., vol. 9, no. 3, pp. 81-84, Mar. 2002.

[18] J. A. Jensen, "A model for the propagation and scattering of ultrasound tissue," *J. Acoust. Soc. Am*., vol. 89, pp. 182-190, Jan. 1991.

[19] W. Wu, S. T. Acton, J. Lack, "Real-time processing of ultrasound images with speckle reducing anisotropic diffusion," *ACSSC '06, Fortieth Asilomar Conference on Signals, Systems and Computers*, pp.1458-1464, 2006.

Joshua S. Ullom was born in Normal, IL, USA, in 1988. He earned his B.S. degree in electrical engineering with computer option in 2010 from Bradley University, Peoria, IL.

Mr. Ullom worked in a practicum program with Caterpillar, Inc. from 2008-2009. As a senior, he was on the executive board of the Bradley University student chapter of IEEE. His research interests include image processing, signal processing, and software algorithmic design. As of 2010, he has accepted a position with Harris Corporation as a Software Engineer.